Classification of Hyper-scale Multimodal Imaging Datasets

Craig MacFadyen[1] Ajay Duraiswamy[1] David Harris-Birtill[1*]

[1]University of St Andrews, St Andrews, United Kingdom

Abstract

Algorithms that can classify hyper-scale multi-modal datasets, comprising of millions of images, into constituent modality types can help researchers quickly retrieve and classify diagnostic imaging data, accelerating clinical outcomes. This research aims to demonstrate that a deep neural network that is trained on a hyper-scale dataset (4.5 million images) composed of heterogeneous multi-modal data, can be used to obtain significant modality classification accuracy (96%). By combining 102 medical imaging datasets, a dataset of 4.5 million images was created. A ResNet-50, ResNet-18 and VGG16 were trained to classify these images by the imaging modality used to capture them (Computed Tomography (CT), Magnetic Resonance Imaging (MRI), Positron Emission Tomography (PET), and X-ray) across many body locations. The classification accuracy of the models was then tested on unseen data.

The best performing model achieved classification accuracy of 96% on unseen data. The model achieved a balanced accuracy of 86%.

This research shows it is possible to train Deep Learning (DL) Convolutional Neural Networks (CNNs) with hyper-scale multimodal data-sets, composed of millions of images. The trained model can be used to classify images by modality, with the best performing model achieving a classification accuracy of 96%. Such models can find use in real-world applications with volumes of image data in the hyper-scale range, such as medical imaging repositories, or national healthcare institutions. Further research can expand this classification capability to include 3D-scans.

1 Introduction

With the proliferation of deep neural networks trained on heterogenous multimodal data to detect and predict diseases, there has been an explosion in the volume of diagnostic medical imaging data [1]. Clinicians often order multiple scans of the same patient in different modalities to gather evidence to make improved diagnosis/prognosis [2]. Algorithms that can accurately classify a large hetergogenous dataset into its constituent modalities can be beneficial to researchers and clinicians, allowing them to automatically segment a particular

*Corresponding author email: dcchb@st-andrews.ac.uk

type of modality for retrieval, archival, data balancing, and diagnostic purposes. Manual methods for classifying medical images are typically error-prone unless done by costly domain experts [3].

This paper outlines an deep neural network that accurately classifies a hyper-scale (4.5 million images), mixed-modality dataset into constituent modalities. The developed approach has significant benefit potential for researchers, clinicians, and imaging archives by helping effectively and efficiently classify diagnostic imaging data, in the magnitude of real-world volumes. While classification of hyperscale datasets have been attempted in other areas, such as Earth-science[4], including studies of plankton and marine snow [5], and XYZ, the proposed approach is novel in the field of classification of medical imaging modalities. This study aims to stimulate other hyper-scale projects in this area.

Figure 1: Visualisation of a spread of images from different locations in different modalities. Different modalities use different kinds of radiation, and these are absorbed to varying degrees by tissue in the human body. This leads to the same tissue looking different in each modality. Examples of modalities showing variation of the same tissue: [6] [7] [8] [9] [10] [11] [12] [13] [14] [14] [15]

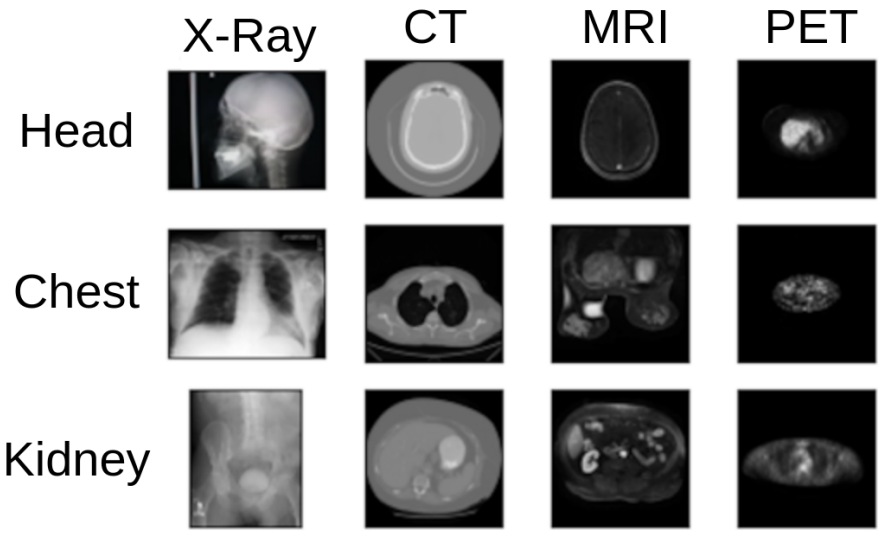

Multiple open-access data sets were used to build the hyper-scale multimodal dataset of 4.5 million images from sources such as The Cancer Imaging Archive [16], Stanford ML Group[17] the largest of which contains 262,000 chest X-ray images, and Kaggle [18] host labelled datasets.

Figure 2: XXX

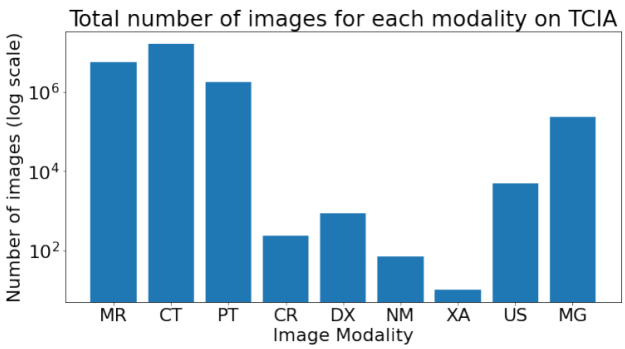

The models trained on this hyper-scale multimodal dataset were a ResNet-18,23 ResNet-50 and a VGG16. When these models were tested for classification accuracy, these results are in the high 90%'s across the train, validate and test sets which shows that the models are able to classify with significant accuracy. Table 1 shows the accuracy and balanced accuracy of each of the models on the test set. Figure 6 shows the confusion matrix for the ResNet18, the best performing of the models tested in this study. The confusion matrix shows that the model demonstrates significant classification performance (96%+) on classifying CT, MR and PET modalities.

1.1 Previous Literature

A number of research articles focus on deep learning systems to classify modalities in diagnostic imaging data. However, to the best of our knowledge,there have not been any examples of a system that combines medical imaging datasets at the hyper-scale (millions of images) level to perform modality classification.

Approaches to classifying medical imaging data by modality primarily take two forms (1) hand-crafted features, and (2) Deep Learning.

The early approaches were based on hand-crafted features, such as picking a specific texture and colour[19], SIFT descriptors[20], bag-of-colours[21] and then using SVM [22], KNN [23] as the classifier[24]. These approaches were limited by the choice of features, and limited accuracy[3]. Further, typically high computational costs inherently limit the size of the datasets used.

A number of approaches using deep learning classifiers are seen in literature. However, all approaches reviewed were seen to be utilising a limited dataset volumes with sizes in the lower order of magnitude, typically hundreds to thousands ($10^2 - 10^3$) of images. Therefore, real-world classification performance of these algorithms when operated on typical image-repository scales of millions of images is unknown.

Chiang et al. use a dataset of 2,878 images to train a CNN classifier on 4 modalities[25], Abdominal CT, Brain CT, Lumbar Spine MRI, and Brain MRI, achieving an average validation accuracy of $> 99.5\%$. Cheng et al. use a cascaded CNN to classify a bimodal dataset, comprised of MRI and PET images[26]. Using a dataset in the order of 10^2 images, they achieved a classification accuracy of 89.6%. Yu et al. use a DNN, and a dataset from the ImageCLEF database, comprising of 2,901 training and 2,582 test images to demonstrate a best classification accuracy of 70%[27]. Sevakula et al. use transfer learning to compare performance of seven DCNNs[28]. Using a curated dataset of 5,500 images from the Open-i Biomedical Image Search Engine, they achieve a best classification accuracy of 99.45% on the Inception-V3 network. Finally, Trenta et al. use a dataset comprised of 8,500 slices and a test set of 1,320 slices (split across 5 classes), and transfer learning techniques to achieve an overall accuracy of upto 100% on specific modalities, on their pre-trained VGGNet implementation[24].

Summarising classification performance figures reported in extant literature:

To summarise, two thing are evident, (1) deep learning learning models present several advantages over handcrafted, feature driven models, and (2) it is seen that the largest of the datasets in the literature reviewed is in the order of 10^3 images. Given that image repositories are now typically in the hyper-scale order, and growing rapidly, a suitably trained CNN capable of handling hyper-scale datasets is required.

Table 1: Dataset sizes vs Performance

Study	Dataset Magnitude	Classifier Accuracy
Chiang et al.[25]	10^3	$> 99.5\%$
Cheng et al.[26]	10^2	$> 89.6\%$
Yu et al.[27]	10^3	70%
Sevakula et al.[28]	10^3	99.45%
Trenta et al.[24]	10^3	100%

2 Materials & Methods

2.1 Data

In total, 102 datasets were downloaded and combined to form an hyper-scale image dataset of 4.5 million images. The full list of datasets with citations is provided in Appendix A. Four modalities were selected as targets for the classification task; CT, MRI, X-ray and PET. Other modalities (e.g. ultrasound) were excluded from this study because of a lack of appreciable volumes of data. The main source of this data was the Cancer Imaging Archive (TCIA) [16]. The Cancer Imaging Archive provides a REST API that allows for programmatic retrieval of images which allowed data to be downloaded and combined easily, and in a reproducible way. However, because the Cancer Imaging Archive's main purpose is to host datasets relating to cancer research it was important to seek out some extra datasets to augment the data TCIA provides. The full list of datasets can be found in Appendix A.

This project was approved by the University of St Andrews University Teaching and Research Ethics Committee (UTREC), approval code CS15171.

2.2 Train-Validate-Test Split

The downloaded data was split into three separate parts - train, validate and test. The train set was used to train the model, the validate set was used to evaluate the models between training runs, and the test set was used once to evaluate the final trained models. It was important to create the splits at the dataset level to prevent data-leakage. That is, all the images from a dataset were placed in the same split. Scans of the same patient in the same modality are likely to be similar, so if there is an image of the same patient in the train and test set then the test set does not contain completely unseen data. Putting each dataset into one of train, validate or test prevents this data leakage. Splitting the datasets like this also helps achieve the goal of demonstrating generalisation across datasets, because no dataset in the train set is represented in the test set.

The train-validate-test split was created manually to ensure as even a spread as possible of images for each modality and location in each split. The manual split ensured that there are at least two locations for each

modality in each of the train, validate and test split. The main difficulty for this was X-rays, because in the TCIA datasets most X-rays are mammograms. This meant the non-TCIA datasets had to be carefully split. Again, Appendix A shows the split each dataset was placed in. Figure 3c shows the number of images in the train, validate and test set. TCIA hosts many CT and MR datasets and some of these datasets are very large. For example, the CT Colonography dataset [29] has more than 900,000 CT images, which is more than the total number of X-ray images across all datasets used in this study. To ensure the other modalities were not completely dwarfed by these datasets, a maximum of 50,000 CT images and 100,000 MR images was taken from each individual dataset. The images were selected in the order given by TCIA. This selection method was not applied to the images from sources other than TCIA. After imbalance correction, the total number of images in the dataset were 6,433,838 (6.4 million images), with a spilt of 4,104,184 in training, 936,347 in test, and 1,393,307 in validate datasets.

2.3 Preprocessing

In order for 2D and 3D scans to be used in the same study, the 3D scans (CT, MR and PT) were treated as a collection of 2D images. These images are sometimes referred to as slices. The images were resized to 224×224 and rescaled between 0 and 1. Each image was rescaled using min-max normalisation with the maximum and minimum values being the highest and lowest pixel values present within the image.

2.4 Network Architecture and Training

The models trained on this dataset were a ResNet-18 [30], ResNet-50 and a VGG16 [31]. The code used was adapted from PyTorch's hosted versions of these models[32]. Changes were made to the channel depth of the input layer, from three channels to one channel (grayscale). These three models were chosen because they have all been shown to perform well when trained with large quantities of data on the ImageNet dataset [30, 31]. The code created as part of this research is open-source and hosted online at Github [33].

All models were trained for 10 epochs with a batch size of 128. The training set contained 2,954,097 ($2.9x10^6$) samples and the validate set contained 704,685 samples. The models were optimised using stochastic gradient descent, with a learning rate of 0.1 that was divided by 10 every time the loss plateaued, a momentum of 0.9 and an L2 weight decay penalty of 0.005. The models were trained on a machine with an Intel(R) Xeon(R) CPU E5-1650 v4 @3.60GHz with 6 physical cores (12 threads), 250GB of RAM and two Nvidia GeForce GTX 1080Tis.

Figure 3: Figures showing the number of images for each modality in the created splits: a) train, b) validate and c) test. Note that each graph has a different scale, the purpose is to show the ratios of each class are similar. There are 73 datasets in the train set, 13 in the validate set and 16 in the test set.

(a) Number of images for each modality in the created train set.

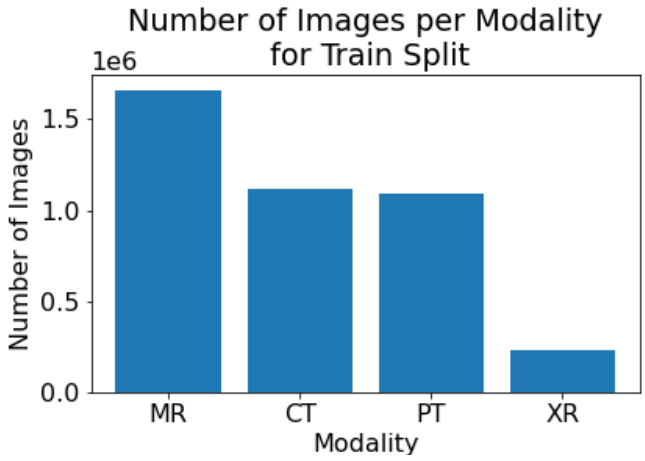

(b) Number of images for each modality in the created validate set.

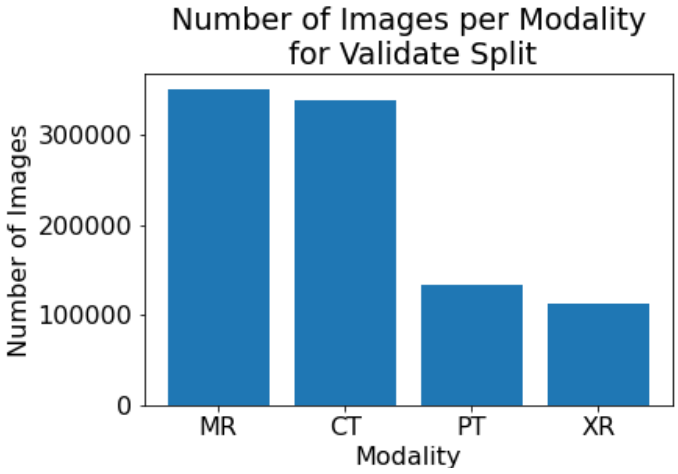

(c) Number of images for each modality in the created test set.

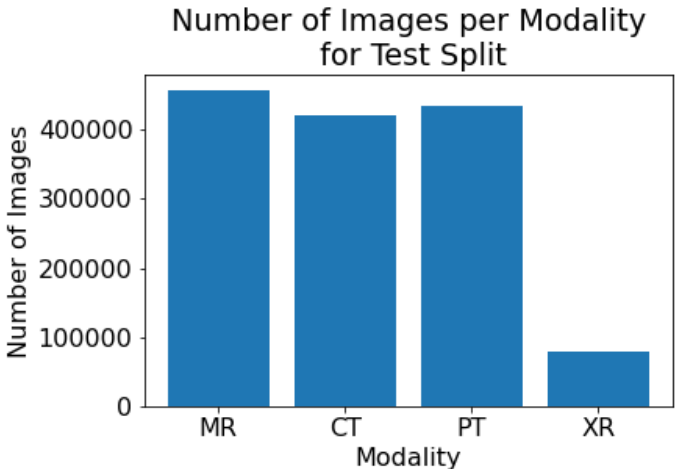

3 Results & Discussion

3.1 Training and Validation Accuracy

Figures 4, shows the training and validation accuracy curves for the ResNet50, ResNet18 and VGG16 models. The small gap between the training and validation accuracies suggests that the models are not overfitting. Figure 5 shows the time it took to train the models over the 10 epochs.

Figure 4: Training and validation accuracy each of the three networks, found at the end of each epoch. The small gap between the training and validation accuracies suggests that the models are not overfitting. Note the scale starts at 90%.

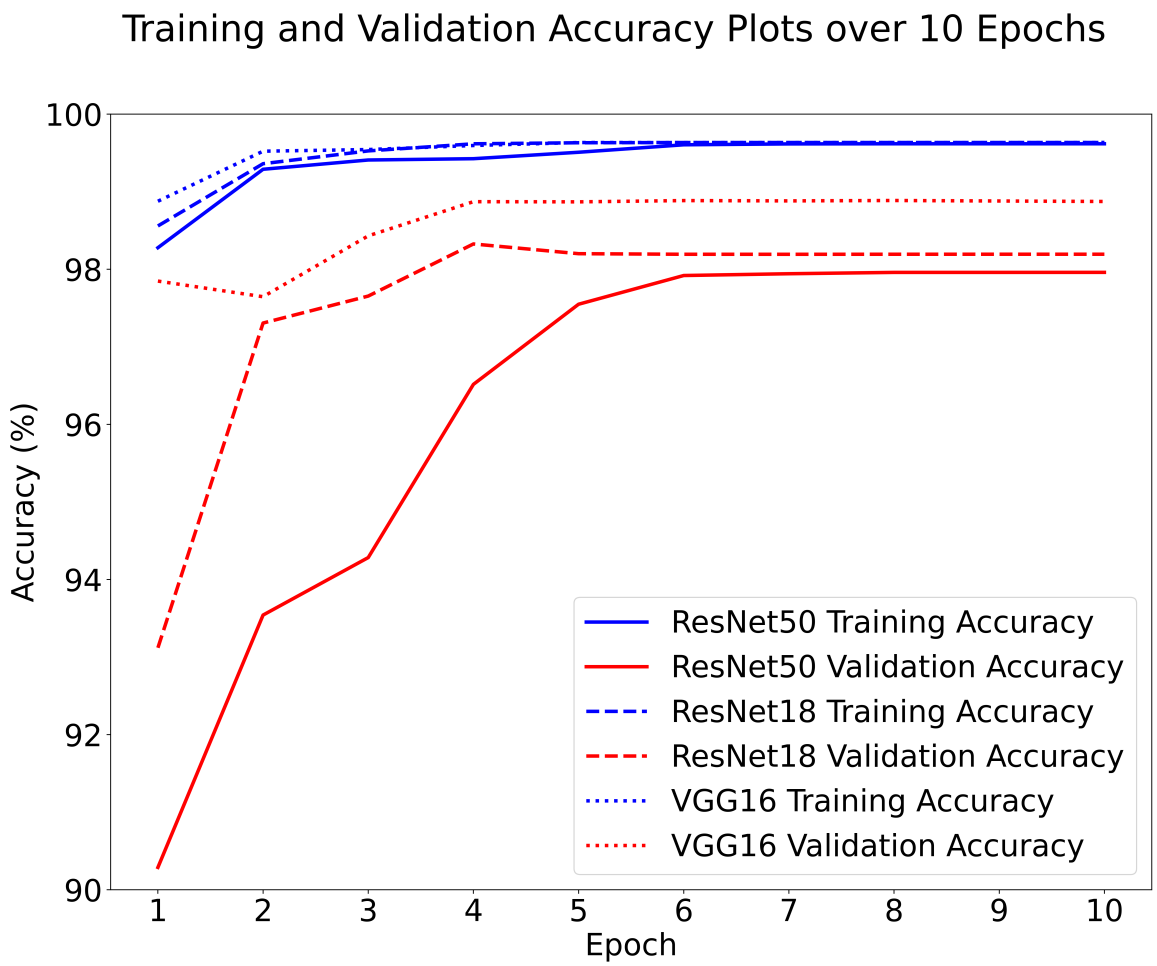

3.2 Test Set Accuracy

Figure 6 shows the accuracy of the three models. These results are in the high 90%'s across the train, validate and test sets which shows that the models have all learned the problem well. Table 2 shows the accuracy and balanced accuracy of each of the models on the test set. Figure 7 shows the confusion matrix for the ResNet18 model. The confusion matrix shows that the model performs very well on CT, MR and PET. Accuracy for X-rays can be improved by adding additional X-ray images across a larger spread of locations.

Figure 5: Time in hours to train the models for 10 epochs.The training and validation accuracy both level-off around epochs 5–6 which shows that the models are able to fit the data.

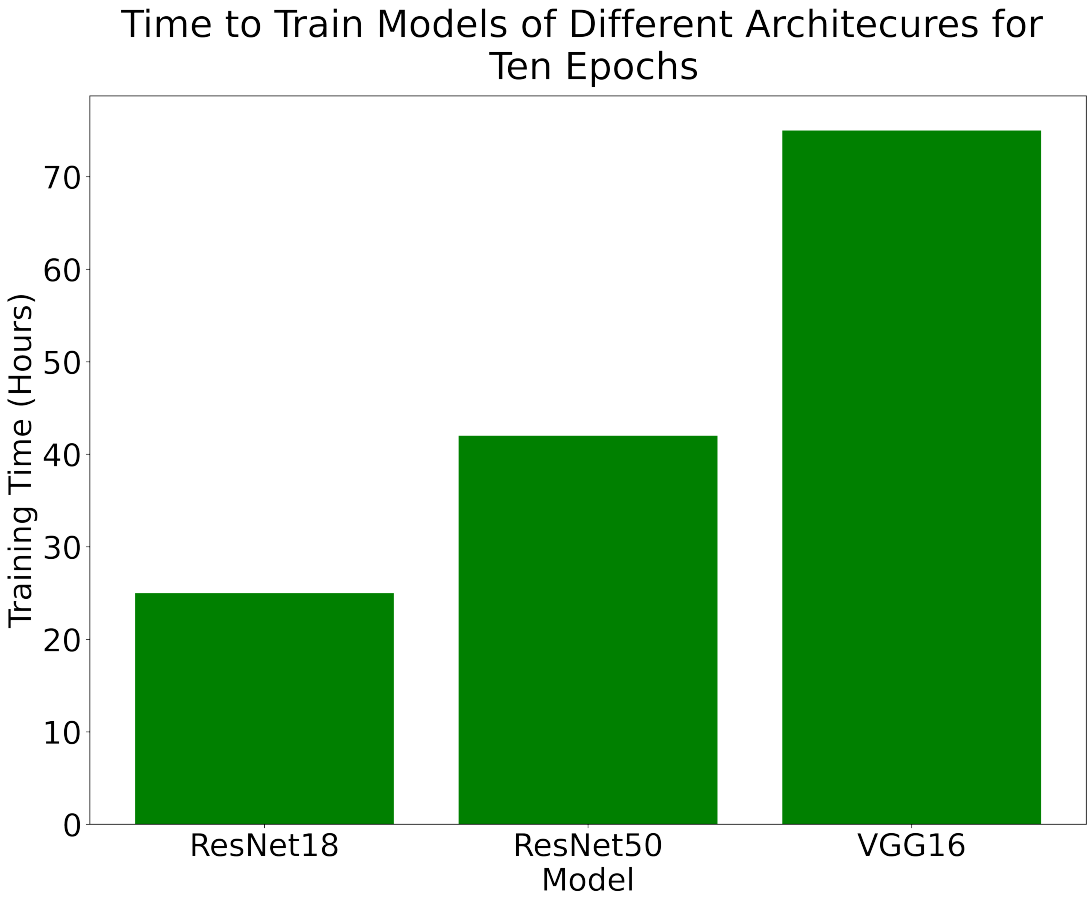

Model	Accuracy	Balanced Accuracy
ResNet18	96.00%	86.17%
ResNet50	95.60%	85.65%
VGG16	94.58%	81.08%

Table 2: Table containing the accuracy and balanced accuracy of various models on the test set. Each model was trained for 10 epochs.

3.3 Dataset Level Results

Table 3 shows the accuracy of the model on each dataset in the test set for the ResNet18 model, chosen because this model demonstrated superior classification performance over others tested in this study. It is interesting to note that in both tables the X-ray performance is in the 80-90% range for the Cancer Imaging Archive X-ray datasets, then drops for the MURA and Osteoarthritis Initiative datasets. This is likely because these datasets are bone X-rays, and most of the datasets only contain chest X-rays. Therefore, a better spread of X-ray datasets is needed for the performance of these models to be improved.

Figure 6: Accuracy of 3 models on the test set.

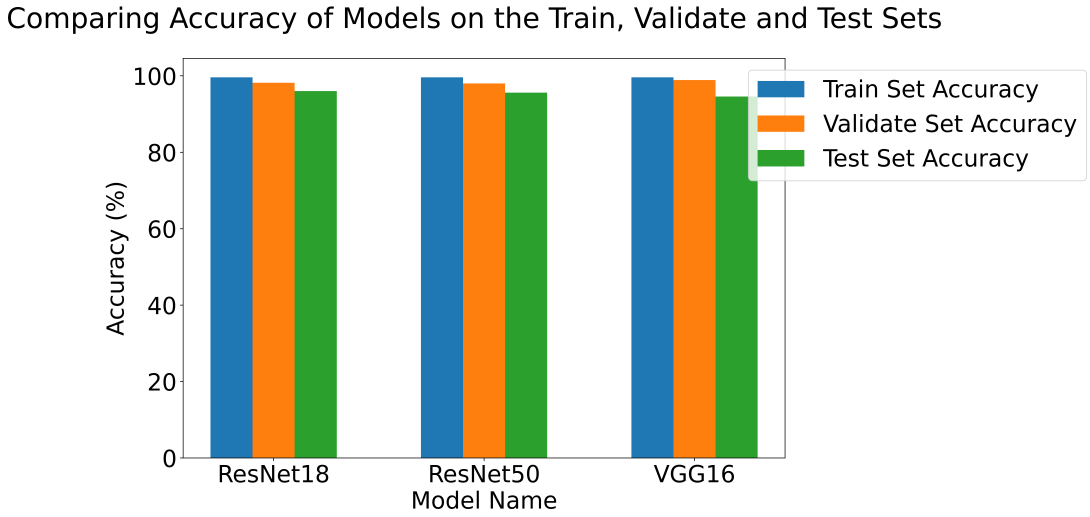

Figure 7: The confusion matrix for the ResNet18 on the test set. The model gains very high accuracy on the CT, MRI and PET. The ResNet18 results were chosen for this plot as this model achieved the highest accuracy and highest balanced accuracy.

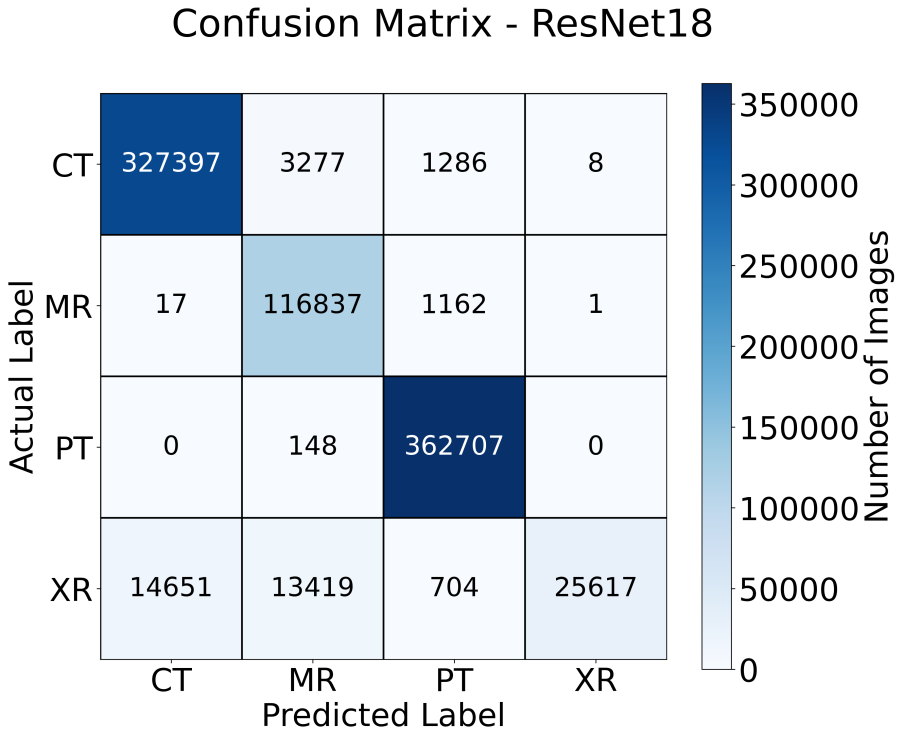

Table 3: Table containing the accuracy of the ResNet18 model on every dataset in the test set. Some datasets appear more than once in this table because they contain multiple image modalities.

Dataset (Location)	Modality	Accuracy (%)
CPTAC-LUAD (Chest)	CT	99
Pelvic-Reference-Data(Pelvis)	CT	81
C4KC-KiTS (Kidney)	CT	100
Anti-PD-1 Lung (Chest)	CT	97
CPTAC-PDA (Pancreas)	CT	100
NaF PROSTATE (Prostate)	CT	100
TCGA-READ (Kidney)	CT	100
QIN-HEADNECK (Head)	CT	100
CPTAC-LSCC (Chest)	CT	100
CPTAC-CCRCC (Kidney)	CT	100
CPTAC-LUAD (Chest)	MR	100
ISPY1 (Breast)	MR	99
Brain-Tumor-Progression (Head)	MR	92
REMBRANDT (Head)	MR	100
BraTS20 (Head)	MR	97
CPTAC-PDA (Pancreas)	MR	99
TCGA-READ (Kidney)	MR	98
CPTAC-CCRCC (Kidney)	MR	99
CPTAC-LUAD (Chest)	PT	100
Anti-PD-1 Lung (Chest)	PT	100
QIN-HEADNECK (Head)	PT	100
CPTAC-PDA (Pancreas)	PT	100
NaF PROSTATE (Prostate)	PT	100
CPTAC-LSCC (Chest)	PT	100
CPTAC-LUAD (Chest)	XR	100
CPTAC-PDA (Pancreas)	XR	96
CPTAC-LSCC (Chest)	XR	92
CPTAC-CCRCC (Kidney)	XR	100
MURA (Bone)	XR	28
Osteo-Arthritis Initiative (Bone)	XR	62

4 Conclusion

In this work, we proposed a hyper-scale classifier, capable of classifying diagnostic imaging data in the scale of millions of medical images, with significant classification accuracy. We used a dataset comprised of 4.5 million images to train a ResNet-50, ResNet-18, and VGG16 CNN. The trained classifiers were then tested for their classification accuracy on 4 modalities ((Computed Tomography (CT), Magnetic Resonance Imaging (MRI), Positron Emission Tomography (PET), and X-ray). The best performing model, among the ones tested demonstrated a classification accuracy of 96%. Our results show that hyper-scale classifiers are capable of accurately classifying volumes of image data encountered in real-word applications, such as those contained in image repositories or diagnostic imaging data collected by national healthcare institutions.

Future work on this topic will be to extend the scope of the hyper-scale modality classifier to work on 3D scan modalities, such as CT, MR, PET.

A List of All Datasets Used

Name	Dataset Webpage	Citations	Split
ACRIN-DSC-MR-Brain	https://doi.org/10.7937/tcia.2019.zr1pjf4i	[7]	Train
Head-Neck-Radiomics-HN1	https://doi.org/10.7937/tcia.2019.8kap372n	[34]	Train
Lung-PET-CT-Dx	https://doi.org/10.7937/TCIA.2020.NNC2-0461	[10]	Train
AAPM RT-MAC Grand Ch. 2019	https://doi.org/10.7937/tcia.2019.bcfjqfqb	[35]	Train
COVID-19-AR	https://doi.org/10.7937/tcia.2020.py71-5978	[36]	Train
CPTAC-CM	https://doi.org/10.7937/K9/TCIA.2018.ODU24GZE	[13]	Train
CPTAC-HNSCC	https://doi.org/10.7937/K9/TCIA.2018.UW45NH81	[37]	Train
PDMR-997537-175-T	https://doi.org/10.7937/TCIA.2020.BRY9-4N29	[38]	Train
PDMR-292921-168-R	https://doi.org/10.7937/TCIA.2020.PCAK-8Z10	[38]	Train
PDMR-425362-245-T	https://doi.org/10.7937/TCIA.2020.7YRS-7J97	[38]	Train
HNSCC	https://doi.org/10.7937/k9/tcia.2020.a8sh-7363	[39, 40]	Train
DRO Toolkit	https://doi.org/10.7937/t062-8262	[41]	Train
QIN GBM Treatment Response	https://doi.org/10.7937/K9/TCIA.2016.nQF4gpn2	[42]	Train
CPTAC-GBM	https://doi.org/10.7937/K9/TCIA.2018.3RJE41Q1	[43]	Train
CPTAC-SAR	https://doi.org/10.7937/TCIA.2019.9bt23r95	[44]	Train
CPTAC-UCEC	https://doi.org/10.7937/K9/TCIA.2018.3R3JUISW	[45]	Train
OPC-Radiomics	https://doi.org/10.7937/tcia.2019.8dho2gls	[46]	Train
Acrin-FLT-Breast (ACRIN 6688)	https://doi.org/10.7937/K9/TCIA.2017.o120zmxg	[8]	Train
QIN-Breast	https://doi.org/doi:10.7937/K9/TCIA.2016.21JUebH0	[47]	Train
Lung Fused-CT-Pathology	https://doi.org/10.7937/K9/TCIA.2018.SMT36LPN	[48]	Train
NSCLC-Radiomics	https://doi.org/10.7937/K9/TCIA.2015.PF0M9REI	[34]	Train
NSCLC-Radiomics-Interobserver1	https://doi.org/10.7937/tcia.2019.cwvlpd26	[49, 34]	Train
PDMR-BL0293-F563	https://doi.org/10.7937/tcia.2019.b6u7wmqw	[38]	Train

Name	Dataset Webpage	Citations	Split
QIN-BRAIN-DSC-MRI	https://doi.org/doi:10.7937/K9/TCIA.2016.5DI84Js8	[50]	Train
CC-Radiomics-Phantom	https://doi.org/10.7937/K9/TCIA.2017.zuzrml5b	[51]	Train
CC-Radiomics-Phantom-2	https://doi.org/10.7937/TCIA.2019.4l24tz5g	[51]	Train
CC-Radiomics-Phantom-3	https://doi.org/10.7937/tcia.2019.j71i4fah	[51]	Train
LCTSC	https://doi.org/10.7937/K9/TCIA.2017.3r3fvz08	[52]	Train
Anti-PD-1 MELANOMA	https://doi.org/10.7937/tcia.2019.1ae0qtcu	[53]	Train
TCGA-UCEC	https://doi.org/10.7937/K9/TCIA.2016.GKJ0ZWAC	[54]	Train
TCGA-HNSC	https://doi.org/10.7937/K9/TCIA.2016.LXKQ47MS	[55]	Train
HNSCC-3DCT-RT	https://doi.org/10.7937/K9/TCIA.2018.13upr2xf	[56]	Train
MRI-DIR	https://doi.org/10.7937/K9/TCIA.2018.3f08iejt	[57]	Train
Head-Neck-PET-CT	https://doi.org/10.7937/K9/TCIA.2017.8oje5q00	[58]	Train
LGG-1p19qDeletion	https://doi.org/10.7937/K9/TCIA.2017.dwehtz9v	[59]	Train
CBIS-DDSM	https://doi.org/10.7937/K9/TCIA.2016.7O02S9CY	[60]	Train
Phantom FDA	https://doi.org/10.7937/K9/TCIA.2015.ORBJKMUX	[61]	Train
QIN LUNG CT	https://doi.org/10.7937/K9/TCIA.2015.NPGZYZBZ	[62]	Train
Mouse-Astrocytoma	https://doi.org/10.7937/K9TCIA.2017.SGW7CAQW	[63]	Train
TCGA-LUSC	https://doi.org/10.7937/K9/TCIA.2016.TYGKKFMQ	[64]	Train
TCGA-LUAD	https://doi.org/10.7937/K9/TCIA.2016.JGNIHEP5	[64]	Train
TCGA-KIRP	https://doi.org/10.7937/K9/TCIA.2016.ACWOGBEF	[15]	Train
TCGA-LIHC	https://doi.org/10.7937/K9/TCIA.2016.IMMQW8UQ	[65]	Train
IvyGAP	https://doi.org/10.7937/K9/TCIA.2016.XLwaN6nL	[66]	Train
Prostate Fused-MRI-Pathology	https://doi.org/10.7937/K9/TCIA.2016.TLPMR1AM	[67, 68, 69, 70]	Train
TCGA-PRAD	https://doi.org/10.7937/K9/TCIA.2016.YXOGLM4Y	[71]	Train
Breast-MRI-NACT-Pilot	https://doi.org/10.7937/K9/TCIA.2016.QHSYHJKY	[72]	Train
RIDER Neuro MRI	https://doi.org/10.7937/K9/TCIA.2015.VOSN3HN1	[73]	Train
Soft-tissue-Sarcoma	https://doi.org/10.7937/K9/TCIA.2015.7GO2GSKS	[74]	Train
Mouse-Mammary	https://doi.org/10.7937/K9/TCIA.2015.9P42KSE6	[75]	Train
TCGA-THCA	https://doi.org/10.7937/K9/TCIA.2016.9ZFRVF1B	[76]	Train
TCGA-SARC	https://doi.org/10.7937/K9/TCIA.2016.CX6YLSUX	[77]	Train
LungCT-Diagnosis	https://doi.org/10.7937/K9/TCIA.2015.A6V7JIWX	[78]	Train
TCGA-CESC	https://doi.org/10.7937/K9/TCIA.2016.SQ4M8YP4	[79]	Train
TCGA-OV	https://doi.org/10.7937/K9/TCIA.2016.NDO1MDFQ	[80]	Train
TCGA-COAD	https://doi.org/10.7937/K9/TCIA.2016.HJJHBOXZ	[76]	Train
TCGA-KIRC	https://doi.org/10.7937/K9/TCIA.2016.V6PBVTDR	[14]	Train
TCGA-LGG	https://doi.org/10.7937/K9/TCIA.2016.L4LTD3TK	[81]	Train
QIN PET Phantom	https://doi.org/10.7937/K9/TCIA.2015.ZPUKHCKB	[82]	Train
QIN Breast DCE-MRI	https://doi.org/10.7937/K9/TCIA.2014.A2N1IXOX	[83]	Train
NSCLC-Radiomics-Genomics	https://doi.org/10.7937/K9/TCIA.2015.L4FRET6Z	[34]	Train
Lung Phantom	https://doi.org/10.7937/K9/TCIA.2015.08A1IXOO	[84]	Train
TCGA-KICH	https://doi.org/10.7937/K9/TCIA.2016.YU3RBCZN	[85]	Train
TCGA-GBM	https://doi.org/10.7937/K9/TCIA.2016.RNYFUYE9	[86]	Train
SPIE-AAPM Lung CT Challenge	https://doi.org/10.7937/K9/TCIA.2015.UZLSU3FL	[87]	Train
Prostate-3T	https://doi.org/10.7937/K9/TCIA.2015.QJTV5IL5	[88]	Train

Name	Dataset Webpage	Citations	Split
Prostate-Diagnosis	https://doi.org/10.7937/K9/TCIA.2015.FOQEUJVT	[89]	Train
RIDER Phantom PET-CT	https://doi.org/10.7937/K9/TCIA.2015.8WG2KN4W	[90]	Train
RIDER Lung CT	https://doi.org/10.7937/K9/TCIA.2015.U1X8A5NR	[91]	Train
RIDER Phantom MRI	https://doi.org/10.7937/K9/TCIA.2015.MI4QDDHU	[92]	Train
RIDER Breast MRI	https://doi.org/10.7937/K9/TCIA.2015.H1SXNUXL	[93]	Train
CT Colonography (ACRIN 6664)	https://doi.org/10.7937/K9/TCIA.2015.NWTESAY1	[29]	Train
Chexpert	https://stanfordmlgroup.github.io/competitions/chexpert/	[9]	Train
RSNA Bone Age	https://www.kaggle.com/kmader/rsna-bone-age	None	Train
TCGA-BRCA	https://doi.org/10.7937/K9/TCIA.2016.AB2NAZRP	[11]	Validate
Acrin-FMISO-Brain (ACRIN 6684)	https://doi.org/10.7937/K9/TCIA.2018.vohlekok	[6]	Validate
TCGA-BLCA	https://doi.org/10.7937/K9/TCIA.2016.8LNG8XDR	[76]	Validate
Pancreas-CT	https://doi.org/10.7937/K9/TCIA.2016.tNB1kqBU	[94]	Validate
CT Lymph Nodes	https://doi.org/10.7937/K9/TCIA.2015.AQIIDCNM	[95]	Validate
TCGA-ESCA	https://doi.org/10.7937/K9/TCIA.2016.VPTNRGFY	[96]	Validate
TCGA-STAD	https://doi.org/10.7937/K9/TCIA.2016.GDHL9KIM	[97]	Validate
LIDC-IDRI	https://doi.org/10.7937/K9/TCIA.2015.LO9QL9SX	[98]	Validate
QIBA CT-1C	https://doi.org/10.7937/K9/TCIA.2016.YxgR4blU	[99]	Validate
RIDER Lung PET-CT	https://doi.org/10.7937/K9/TCIA.2015.OFIP7TVM	[12]	Validate
Prostate-MRI	https://doi.org/10.7937/K9/TCIA.2016.6046GUDv	[100]	Validate
NIH 100000 Chest X-ray	https://nihcc.app.box.com/v/ChestXray-NIHCC	[101]	Validate
MRNet: Knee MRIs	https://stanfordmlgroup.github.io/competitions/mrnet/	[102]	Validate
CPTAC-CCRCC	https://doi.org/10.7937/K9/TCIA.2018.OBLAMN27	[103]	Test
C4KC-KiTS	https://doi.org/10.7937/TCIA.2019.IX49E8NX	[104]	Test
CPTAC-LSCC	https://doi.org/10.7937/K9/TCIA.2018.6EMUB5L2	[105]	Test
LDCT-and-Projection-data	https://doi.org/10.7937/9npb-2637	[106]	Test
CPTAC-LUAD	https://doi.org/10.7937/K9/TCIA.2018.PAT12TBS	[107]	Test
CPTAC-PDA	https://doi.org/10.7937/K9/TCIA.2018.SC20FO18	[108]	Test
Pelvic-Reference-Data	https://doi.org/10.7937/TCIA.2019.woskq5oo	[109]	Test
Anti-PD-1 Lung	https://doi.org/10.7937/tcia.2019.zjjwb9ip	[110]	Test
ISPY1 (ACRIN 6657)	https://doi.org/10.7937/K9/TCIA.2016.HdHpgJLK	[111]	Test
QIN-HeadNeck	https://doi.org/10.7937/K9/TCIA.2015.K0F5CGLI	[112]	Test
TCGA-READ	https://doi.org/10.7937/K9/TCIA.2016.F7PPNPNU	[113]	Test
NaF Prostate	https://doi.org/10.7937/K9/TCIA.2015.ISOQTHKO	[114]	Test
REMBRANDT	https://doi.org/10.7937/K9/TCIA.2015.588OZUZB	[115]	Test
MURA	https://stanfordmlgroup.github.io/competitions/mura/	[116]	Test
NDA Osteoarthritis Initiative	https://nda.nih.gov/oai/	None	Test
BraTS20	http://braintumorsegmentation.org/	None	Test

Code, Data, & Materials Availability

The data used in this study comes from multiple sources, as indicated in Appendix A. If not specified here then the data can be accessed with no special permission required by the data provider. Permission was required to access MURA, ChexPERT, MRNet, the NDA Osteo-Arthritis Initiative and BraTS20.

Code created for this research is hosted on GitHub with an MIT Licence[33].

References

[1] Hafizović, L., Čaušević, A., Deumić, A., Bećirović, L. S., Pokvić, L. G., and Badnjević, A., "The use of artificial intelligence in diagnostic medical imaging: Systematic literature review," in [*2021 IEEE 21st International Conference on Bioinformatics and Bioengineering (BIBE)*], 1–6, IEEE (2021).

[2] Bhatnagar, G., Wu, Q. J., and Liu, Z., "A new contrast based multimodal medical image fusion framework," *Neurocomputing* **157**, 143–152 (2015).

[3] Hassan, M., Ali, S., Alquhayz, H., and Safdar, K., "Developing intelligent medical image modality classification system using deep transfer learning and lda," *Scientific reports* **10**(1), 1–14 (2020).

[4] Reichstein, M., Camps-Valls, G., Stevens, B., Jung, M., Denzler, J., Carvalhais, N., et al., "Deep learning and process understanding for data-driven earth system science," *Nature* **566**(7743), 195–204 (2019).

[5] Irisson, J.-O., Ayata, S.-D., Lindsay, D. J., Karp-Boss, L., and Stemmann, L., "Machine learning for the study of plankton and marine snow from images," *Ann. Rev. Mar. Sci* **14**, 277–301 (2022).

[6] Gerstner, E. R., Zhang, Z., Fink, J. R., Muzi, M., Hanna, L., Greco, E., Prah, M., Schmainda, K. M., Mintz, A., Kostakoglu, L., et al., "Acrin 6684: assessment of tumor hypoxia in newly diagnosed glioblastoma using 18f-fmiso pet and mri," *Clinical Cancer Research* **22**(20), 5079–5086 (2016).

[7] Boxerman, J. L., Zhang, Z., Safriel, Y., Larvie, M., Snyder, B. S., Jain, R., Chi, T. L., Sorensen, A. G., Gilbert, M. R., and Barboriak, D. P., "Early post-bevacizumab progression on contrast-enhanced MRI as a prognostic marker for overall survival in recurrent glioblastoma: results from the ACRIN 6677/RTOG 0625 Central Reader Study," *Neuro-Oncology* **15**, 945–954 (07 2013).

[8] Kostakoglu, L., Duan, F., Idowu, M. O., Jolles, P. R., Bear, H. D., Muzi, M., Cormack, J., Muzi, J. P., Pryma, D. A., Specht, J. M., et al., "A phase ii study of 3'-deoxy-3'-18f-fluorothymidine pet in the assessment of early response of breast cancer to neoadjuvant chemotherapy: results from acrin 6688," *Journal of Nuclear Medicine* **56**(11), 1681–1689 (2015).

[9] Irvin, J., Rajpurkar, P., Ko, M., Yu, Y., Ciurea-Ilcus, S., Chute, C., Marklund, H., Haghgoo, B., Ball, R. L., Shpanskaya, K. S., Seekins, J., Mong, D. A., Halabi, S. S., Sandberg, J. K., Jones, R., Larson, D. B., Langlotz, C. P., Patel, B. N., Lungren, M. P., and Ng, A. Y., "Chexpert: A large chest radiograph dataset with uncertainty labels and expert comparison," *CoRR* **abs/1901.07031** (2019).

[10] Li, P., Wang, S., Li, T., Lu, J., HuangFu, Y., and Wang, D., "A large-scale ct and pet/ct dataset for lung cancer diagnosis [data set].," *The Cancer Imaging Archive* (2020).

[11] Lingle, W., Erickson, B., Zuley, M., Jarosz, R., Bonaccio, E., Filippini, J., and Gruszauskas, N., "Radiology data from the cancer genome atlas breast invasive carcinoma [tcga-brca] collection," *The Cancer Imaging Archive* (2016).

[12] Muzi, P., Wanner, M., and Kinahan, P., "Data from rider lung pet-ct," *The Cancer Imaging Archive* (2015).

[13] Consortium, N. C. I. C. P. T. A., "Radiology data from the clinical proteomic tumor analysis consortium cutaneous melanoma [cptac-cm] collection," *The Cancer Imaging Archive* (2018).

[14] Akin, O., Elnajjar, P., Heller, M., Jarosz, R., Erickson, B., Kirk, S., and Filippini, J., "Radiology data from the cancer genome atlas kidney renal clear cell carcinoma [tcga-kirc] collection," *The Cancer Imaging Archive* (2016).

[15] Linehan, M., Gautam, R., Kirk, S., Lee, Y., Roche, C., Bonaccio, E., and Jarosz, R., "Radiology data from the cancer genome atlas cervical kidney renal papillary cell carcinoma [kirp] collection," *Cancer Imaging Arch* (2016).

[16] Clark, K., Vendt, B., Smith, K., Freymann, J., Kirby, J., Koppel, P., Moore, S., Phillips, S., Maffitt, D., Pringle, M., et al., "The cancer imaging archive (tcia): maintaining and operating a public information repository," *Journal of digital imaging* **26**(6), 1045–1057 (2013).

[17] Stanford, "Stanford ml group," (2023). https://stanfordmlgroup.github.io/, Last accessed on 2023-01-02.

[18] Kaggle, "Kaggle," (2023). https://www.kaggle.com/, Last accessed on 2023-01-02.

[19] Kalpathy-Cramer, J., Hersh, W., et al., "Automatic image modality based classification and annotation to improve medical image retrieval," in [*Medinfo*], 1334–1338 (2007).

[20] Kitanovski, I., Dimitrovski, I., and Loshkovska, S., "Fcse at medical tasks of imageclef 2013," (2013).

[21] Valavanis, L., Stathopoulos, S., and Kalamboukis, T., "Ipl at clef 2016 medical task.," *CLEF (Working Notes)* **1609**, 413–420 (2016).

[22] Cao, J., Wang, M., Li, Y., and Zhang, Q., "Improved support vector machine classification algorithm based on adaptive feature weight updating in the hadoop cluster environment," *PloS one* **14**(4), e0215136 (2019).

[23] Markonis, D., de Herrera, A. G. S., Eggel, I., and Müller, H., "Multi-scale visual words for hierarchical medical image categorisation," in [*Medical Imaging 2012: Advanced PACS-based Imaging Informatics and Therapeutic Applications*], **8319**, 99–109, SPIE (2012).

[24] Trenta, F., Battiato, S., and Ravì, D., "An explainable medical imaging framework for modality classifications trained using small datasets," in [*International Conference on Image Analysis and Processing*], 358–367, Springer (2022).

[25] Chiang, C.-H., Weng, C.-L., and Chiu, H.-W., "Automatic classification of medical image modality and anatomical location using convolutional neural network," *Plos one* **16**(6), e0253205 (2021).

[26] Cheng, D. and Liu, M., "Classification of alzheimer's disease by cascaded convolutional neural networks using pet images," in [*International Workshop on Machine Learning in Medical Imaging*], 106–113, Springer (2017).

[27] Yu, Y., Lin, H., Yu, Q., Meng, J., Zhao, Z., Li, Y., and Zuo, L., "Modality classification for medical images using multiple deep convolutional neural networks," *J. Comput. Inf. Syst* **11**(15), 5403–5413 (2015).

[28] Sevakula, R. K., Singh, V., Verma, N. K., Kumar, C., and Cui, Y., "Transfer learning for molecular cancer classification using deep neural networks," *IEEE/ACM transactions on computational biology and bioinformatics* **16**(6), 2089–2100 (2018).

[29] Johnson, C. D., Chen, M.-H., Toledano, A. Y., Heiken, J. P., Dachman, A., Kuo, M. D., Menias, C. O., Siewert, B., Cheema, J. I., Obregon, R. G., et al., "Accuracy of ct colonography for detection of large adenomas and cancers," *New England Journal of Medicine* **359**(12), 1207–1217 (2008).

[30] He, K., Zhang, X., Ren, S., and Sun, J., "Deep residual learning for image recognition," *CoRR* **abs/1512.03385** (2015).

[31] Simonyan, K. and Zisserman, A., "Very deep convolutional networks for large-scale image recognition," *arXiv preprint arXiv:1409.1556* (2014).

[32] Pytorch, "Pytorch," (2023). https://pypi.org/project/torchvision/, Last accessed on 2023-01-02.

[33] Craig, MacFadyen and David, Harris-Birtill, "Research code," (2023). https://github.com/cdmacfadyen/classify-modality/, Last accessed on 2023-01-02.

[34] Aerts, H. J., Velazquez, E. R., Leijenaar, R. T., Parmar, C., Grossmann, P., Carvalho, S., Bussink, J., Monshouwer, R., Haibe-Kains, B., Rietveld, D., et al., "Decoding tumour phenotype by noninvasive imaging using a quantitative radiomics approach," *Nature communications* **5**(1), 1–9 (2014).

[35] Cardenas, C. E., Mohamed, A. S., Yang, J., Gooding, M., Veeraraghavan, H., Kalpathy-Cramer, J., Ng, S. P., Ding, Y., Wang, J., Lai, S. Y., et al., "Head and neck cancer patient images for determining auto-segmentation accuracy in t2-weighted magnetic resonance imaging through expert manual segmentations," *Medical Physics* **47**(5), 2317–2322 (2020).

[36] Desai, S., Baghal, A., Wongsurawat, T., Jenjaroenpun, P., Powell, T., Al-Shukri, S., Gates, K., Farmer, P., Rutherford, M., Blake, G., et al., "Chest imaging representing a covid-19 positive rural us population," *Scientific data* **7**(1), 1–6 (2020).

[37] Consortium, N. C. I. C. P. T. A., "Radiology data from the clinical proteomic tumor analysis consortium head and neck squamous cell carcinoma [cptac-hnscc] collection," *The Cancer Imaging Archive* (2018).

[38] Tatum, J. L., Kalen, J. D., Ileva, L. V., Riffle, L. A., Keita, S., Patel, N., Jacobs, P. M., Sanders, C., James, A., Difilippantonio, S., Thang, L., Hollingshead, M. G., Phillips, J., Evrard, Y., Clunie, D. A.and Liu, Y., Suloway, C., Smith, K. E., Wagner, U., and Doroshow, J. H., "Imaging characterization of

a metastatic patient derived model of adenocarcinoma colon: Pdmr-997537-175-t [data set].," *The Cancer Imaging Archive* (2020).

[39] Grossberg, A. J., Mohamed, A. S., Elhalawani, H., Bennett, W. C., Smith, K. E., Nolan, T. S., Williams, B., Chamchod, S., Heukelom, J., Kantor, M. E., et al., "Imaging and clinical data archive for head and neck squamous cell carcinoma patients treated with radiotherapy," *Scientific data* **5**, 180173 (2018).

[40] Elhalawani, H., Mohamed, A. S., White, A. L., Zafereo, J., Wong, A. J., Berends, J. E., AboHashem, S., Williams, B., Aymard, J. M., Kanwar, A., et al., "Matched computed tomography segmentation and demographic data for oropharyngeal cancer radiomics challenges," *Scientific data* **4**, 170077 (2017).

[41] Jaggi, A., Mattonen, S. A., McNitt-Gray, M., and Napel, S., "Stanford dro toolkit: digital reference objects for standardization of radiomic features," *Tomography* **6**(2), 111 (2020).

[42] Prah, M., Stufflebeam, S., Paulson, E., Kalpathy-Cramer, J., Gerstner, E., Batchelor, T., Barboriak, D., Rosen, B., and Schmainda, K., "Repeatability of standardized and normalized relative cbv in patients with newly diagnosed glioblastoma," *American Journal of Neuroradiology* **36**(9), 1654–1661 (2015).

[43] Consortium, N. C. I. C. P. T. A., "Radiology data from the clinical proteomic tumor analysis consortium glioblastoma multiforme [cptac-gbm] collection [data set].," *The Cancer Imaging Archive* (2018).

[44] Consortium, N. C. I. C. P. T. A., "Radiology data from the clinical proteomic tumor analysis consortium sarcomas [cptac-sar] collection [data set].," *The Cancer Imaging Archive* (2018).

[45] Consortium, N. C. I. C. P. T. A., "Radiology data from the clinical proteomic tumor analysis consortium uterine corpus endometrial carcinoma [cptac-ucec] collection [data set].," *The Cancer Imaging Archive* (2018).

[46] Kwan, J. Y. Y., Su, J., Huang, S. H., Ghoraie, L. S., Xu, W., Chan, B., Yip, K. W., Giuliani, M., Bayley, A., Kim, J., et al., "Radiomic biomarkers to refine risk models for distant metastasis in hpv-related oropharyngeal carcinoma," *International Journal of Radiation Oncology* Biology* Physics* **102**(4), 1107–1116 (2018).

[47] Li, X., Abramson, R. G., Arlinghaus, L. R., Kang, H., Chakravarthy, A. B., Abramson, V. G., Farley, J., Mayer, I. A., Kelley, M. C., Meszoely, I. M., et al., "Multiparametric magnetic resonance imaging for predicting pathological response after the first cycle of neoadjuvant chemotherapy in breast cancer," *Investigative radiology* **50**(4), 195–204 (2015).

[48] Rusu, M., Rajiah, P., Gilkeson, R., Yang, M., Donatelli, C., Thawani, R., Jacono, F. J., Linden, P., and Madabhushi, A., "Co-registration of pre-operative ct with ex vivo surgically excised ground glass nodules to define spatial extent of invasive adenocarcinoma on in vivo imaging: a proof-of-concept study," *European radiology* **27**(10), 4209–4217 (2017).

[49] Kalendralis, P., Shi, Z., Traverso, A., Choudhury, A., Sloep, M., Zhovannik, I., Starmans, M. P., Grittner, D., Feltens, P., Monshouwer, R., et al., "Fair-compliant clinical, radiomics and dicom metadata of rider, interobserver, lung1 and head-neck1 tcia collections," *Medical Physics* (2020).

[50] Schmainda, K., Prah, M., Connelly, J., and Rand, S., "Glioma dsc-mri perfusion data with standard imaging and rois," *The Cancer Imaging Archive. http://doi. org/10.7937 K* **9** (2016).

[51] Mackin, D., Fave, X., Zhang, L., Fried, D., Yang, J., Taylor, B., Rodriguez-Rivera, E., Dodge, C., and Jones, A., "Court l," *Data from Credence Cartridge Radiomics Phantom CT Scans. The Cancer Imaging Archive* (2017).

[52] Yang, J., Veeraraghavan, H., Armato III, S. G., Farahani, K., Kirby, J. S., Kalpathy-Kramer, J., van Elmpt, W., Dekker, A., Han, X., Feng, X., et al., "Autosegmentation for thoracic radiation treatment planning: A grand challenge at aapm 2017," *Medical physics* **45**(10), 4568–4581 (2018).

[53] Patnana, M., Patel, S., and Tsao, A., "Anti-pd-1 immunotherapy melanoma dataset [data set].," *The Cancer Imaging Archive* (2019).

[54] Erickson, B. J., Mutch, D., Lippmann, L., and Jarosz, R., "Radiology data from the cancer genome atlas uterine corpus endometrial carcinoma (tcga-ucec) collection," *The Cancer Imaging Archive* (2016).

[55] Zuley, M. L., Jarosz, R., Kirk, S., Lee, Y., Colen, R., Garcia, K., and Aredes, N. D., "Radiology data from the cancer genome atlas head-neck squamous cell carcinoma [tcga-hnsc] collection," *The Cancer Imaging Archive* (2016).

[56] Bejarano, T., De Ornelas-Couto, M., and Mihaylov, I. B., "Longitudinal fan-beam computed tomography dataset for head-and-neck squamous cell carcinoma patients," *Medical physics* **46**(5), 2526–2537 (2019).

[57] Ger, R. B., Yang, J., Ding, Y., Jacobsen, M. C., Cardenas, C. E., Fuller, C. D., Howell, R. M., Li, H., Stafford, R. J., Zhou, S., et al., "Synthetic head and neck and phantom images for determining deformable image registration accuracy in magnetic resonance imaging," *Medical physics* **45**(9), 4315–4321 (2018).

[58] Vallieres, M., Kay-Rivest, E., Perrin, L. J., Liem, X., Furstoss, C., Aerts, H. J., Khaouam, N., Nguyen-Tan, P. F., Wang, C.-S., Sultanem, K., et al., "Radiomics strategies for risk assessment of tumour failure in head-and-neck cancer," *Scientific reports* **7**(1), 1–14 (2017).

[59] Akkus, Z., Ali, I., Sedlář, J., Agrawal, J. P., Parney, I. F., Giannini, C., and Erickson, B. J., "Predicting deletion of chromosomal arms 1p/19q in low-grade gliomas from mr images using machine intelligence," *Journal of digital imaging* **30**(4), 469–476 (2017).

[60] Lee, R. S., Gimenez, F., Hoogi, A., Miyake, K. K., Gorovoy, M., and Rubin, D. L., "A curated mammography data set for use in computer-aided detection and diagnosis research," *Scientific data* **4**, 170177 (2017).

[61] Gavrielides, M. A., Kinnard, L. M., Myers, K. J., Peregoy, J., Pritchard, W. F., Zeng, R., Esparza, J., Karanian, J., and Petrick, N., "A resource for the assessment of lung nodule size estimation methods: database of thoracic ct scans of an anthropomorphic phantom," *Optics express* **18**(14), 15244 (2010).

[62] Kalpathy-Cramer, J., Napel, S., Goldgof, D., and Zhao, B., "Qin multi-site collection of lung ct data with nodule segmentations," *Cancer Imaging Arch* **10**, K9 (2015).

[63] Jansen, S. and Van Dyke, T., "Tcia mouse-astrocytoma collection," *The Cancer Imaging Archive* (2015).

[64] Albertina, B., Watson, M., Holback, C., Jarosz, R., Kirk, S., Lee, Y., and Lemmerman, J., "Radiology data from the cancer genome atlas lung adenocarcinoma [tcga-luad] collection," *The Cancer Imaging Archive* (2016).

[65] Erickson, B., Kirk, S., Lee, Y., Bathe, O., Kearns, M., Gerdes, C., Rieger-Christ, K., and Lemmerman, J., "Radiology data from the cancer genome atlas liver hepatocellular carcinoma [tcga-lihc] collectionthe," *Cancer Imaging Archive* (2016).

[66] Puchalski, R. B., Shah, N., Miller, J., Dalley, R., Nomura, S. R., Yoon, J.-G., Smith, K. A., Lankerovich, M., Bertagnolli, D., Bickley, K., et al., "An anatomic transcriptional atlas of human glioblastoma," *Science* **360**(6389), 660–663 (2018).

[67] Singanamalli, A., Rusu, M., Sparks, R. E., Shih, N. N., Ziober, A., Wang, L.-P., Tomaszewski, J., Rosen, M., Feldman, M., and Madabhushi, A., "Identifying in vivo dce mri markers associated with microvessel architecture and gleason grades of prostate cancer," *Journal of Magnetic Resonance Imaging* **43**(1), 149–158 (2016).

[68] Toth, R. J., Shih, N., Tomaszewski, J. E., Feldman, M. D., Kutter, O., Yu, D. N., Paulus Jr, J. C., Paladini, G., and Madabhushi, A., "Histostitcher™: An informatics software platform for reconstructing whole-mount prostate histology using the extensible imaging platform framework," *Journal of Pathology Informatics* **5** (2014).

[69] Xiao, G., Bloch, B. N., Chappelow, J., Genega, E. M., Rofsky, N. M., Lenkinski, R. E., Tomaszewski, J., Feldman, M. D., Rosen, M., and Madabhushi, A., "Determining histology-mri slice correspondences for defining mri-based disease signatures of prostate cancer," *Computerized Medical Imaging and Graphics* **35**(7-8), 568–578 (2011).

[70] Chappelow, J., Bloch, B. N., Rofsky, N., Genega, E., Lenkinski, R., DeWolf, W., and Madabhushi, A., "Elastic registration of multimodal prostate mri and histology via multiattribute combined mutual information," *Medical Physics* **38**(4), 2005–2018 (2011).

[71] Zuley, M., Jarosz, R., Drake, B., et al., "Radiology data from the cancer genome atlas prostate adenocarcinoma [tcga-prad] collection," *The Cancer Imaging Archive. Available online: http://doi. org/10.7937 K* **9** (2016).

[72] Newitt, D. and Hylton, N., "Single site breast dce-mri data and segmentations from patients undergoing neoadjuvant chemotherapy," *The Cancer Imaging Archive* **2** (2016).

[73] Barboriak, D., "Data from rider neur mri. the cancer imaging archive," (2015).

[74] Vallières, M., Freeman, C. R., Skamene, S. R., and El Naqa, I., "A radiomics model from joint fdg-pet and mri texture features for the prediction of lung metastases in soft-tissue sarcomas of the extremities," *Physics in Medicine and Biology* **60**(14), 5471 (2015).

[75] Jansen, S., Ileva, L., Lu, L., and Van Dyke, T., "Tcia mouse-mammary collection," *The Cancer Imaging Archive* (2015).

[76] Kirk, S., Lee, Y., Roche, C., Bonaccio, E., Filippini, J., and Jarosz, R., "Radiology data from the cancer genome atlas thyroid cancer [tcga-thca] collection," *Cancer Imaging Archive. doi* **10**, K9 (2016).

[77] Roche, C., Bonaccio, E., and Filippini, J., "cited 2019 18/01/2019," *Radiology data from The Cancer Genome Atlas Sarcoma collection. The Cancer Imaging Archive 2016* (2016).

[78] Grove, O., Berglund, A. E., Schabath, M. B., Aerts, H. J., Dekker, A., Wang, H., Velazquez, E. R., Lambin, P., Gu, Y., Balagurunathan, Y., et al., "Quantitative computed tomographic descriptors associate tumor shape complexity and intratumor heterogeneity with prognosis in lung adenocarcinoma," *PloS one* **10**(3), e0118261 (2015).

[79] Lucchesi, F. and Aredes, N., "Radiology data from the cancer genome atlas cervical squamous cell carcinoma and endocervical adenocarcinoma (tcga-cesc) collection. the cancer imaging archive," (2016).

[80] Holback, C., Jarosz, R., Prior, F., Mutch, D. G., Bhosale, P., Garcia, K., and Erickson, B. J., "Radiology data from the cancer genome atlas ovarian cancer [tcga-ov] collection," (2016).

[81] Pedano, N., Flanders, A. E., Scarpace, L., Mikkelsen, T., Eschbacher, J., Hermes, B., and Ostrom, Q., "Radiology data from the cancer genome atlas low grade glioma [tcga-lgg] collection," *The Cancer Imaging Archive* **2** (2016).

[82] Beichel, R. R., Ulrich, E. J., Bauer, C., Byrd, D. W., Muzi, J. P., Muzi, M., and Buatti, J. M., "Data from qin pet phantom," *The Cancer Imaging Archive* (2015).

[83] Huang, W., Li, X., Chen, Y., Li, X., Chang, M.-C., Oborski, M. J., Malyarenko, D. I., Muzi, M., Jajamovich, G. H., Fedorov, A., et al., "Variations of dynamic contrast-enhanced magnetic resonance imaging in evaluation of breast cancer therapy response: a multicenter data analysis challenge," *Translational oncology* **7**(1), 153 (2014).

[84] Zhao, B., "Data from lung phantom," *The Cancer Imaging Archive* (2015).

[85] Linehan, M. W., Gautam, R., Sadow, C. A., and Levine, S., "Radiology data from the cancer genome atlas kidney chromophobe [tcga-kich] collection," *The Cancer Imaging Archive* (2016).

[86] L, S., T, M., Cha and, R. S., S, T., D, G., JH, S., BJ, E., N, P., AE, F., J, B.-S., Q, O., D, B., and LJ, P., "Radiology data from the cancer genome atlas glioblastoma multiforme [tcga-gbm] collection," *The Cancer Imaging Archive* (2016).

[87] Armato III, S. G., Drukker, K., Li, F., Hadjiiski, L., Tourassi, G. D., Engelmann, R. M., Giger, M. L., Redmond, G., Farahani, K., Kirby, J. S., et al., "Lungx challenge for computerized lung nodule classification," *Journal of Medical Imaging* **3**(4) (2016).

[88] Litjens, G., Futterer, J., and Huisman, H., "Data from prostate-3t: the cancer imaging archive," (2015).

[89] Bloch, B. N., Jain, A., and Jaffe, C. C., "Data from prostate-diagnosis," *The Cancer Imaging Archive. Available online: http://doi. org/10.7937 K* **9** (2015).

[90] Muzi, P., Wanner, M., and Kinahan, P., "Data from rider phantom pet-ct," *The Cancer Imaging Archive* (2015).

[91] Zhao, B., James, L. P., Moskowitz, C. S., Guo, P., Ginsberg, M. S., Lefkowitz, R. A., Qin, Y., Riely, G. J., Kris, M. G., and Schwartz, L. H., "Evaluating variability in tumor measurements from same-day repeat ct scans of patients with non–small cell lung cancer," *Radiology* **252**(1), 263–272 (2009).

[92] Jackson, E. F., Barboriak, D. P., Bidaut, L. M., and Meyer, C. R., "Magnetic resonance assessment of response to therapy: tumor change measurement, truth data and error sources," *Translational Oncology* **2**(4), 211 (2009).

[93] Meyer, C. R., Chenevert, T. L., Galbán, C. J., Johnson, T. D., Hamstra, D. A., Rehemtulla, A., and Ross, B. D., "Data from rider-breast-mri. the cancer imaging archive," (2015).

[94] Roth, H. R., Lu, L., Farag, A., Shin, H.-C., Liu, J., Turkbey, E. B., and Summers, R. M., "Deeporgan: Multi-level deep convolutional networks for automated pancreas segmentation," in [*International conference on medical image computing and computer-assisted intervention*], 556–564, Springer (2015).

[95] Roth, H. R., Lu, L., Seff, A., Cherry, K. M., Hoffman, J., Wang, S., Liu, J., Turkbey, E., and Summers, R. M., "A new 2.5 d representation for lymph node detection using random sets of deep convolutional neural network observations," in [*International conference on medical image computing and computer-assisted intervention*], 520–527, Springer (2014).

[96] Lucchesi, F. R. and Aredes, N. D., "Radiology data from the cancer genome atlas esophageal carcinoma [tcga-esca] collection," *The Cancer Imaging Archive* (2016).

[97] Lucchesi, F. and Aredes, N., "Radiology data from the cancer genome atlas stomach adenocarcinoma [tcga-stad] collection, 2016," *The Cancer Imaging Archive* **10**, K9.

[98] Armato III, S. G., McLennan, G., Bidaut, L., McNitt-Gray, M. F., Meyer, C. R., Reeves, A. P., Zhao, B., Aberle, D. R., Henschke, C. I., Hoffman, E. A., et al., "The lung image database consortium (lidc) and image database resource initiative (idri): a completed reference database of lung nodules on ct scans," *Medical physics* **38**(2), 915–931 (2011).

[99] Fenimore, C., McNitt-Gray, M. F., Clunie, D., Gavrielides, M. A., Petrick, N., Samei, E., and Slazak, K., "Data from qiba ct-1c," *The Cancer Imaging Archive* (2016).

[100] P, C., B, T., P, P., M, M., and B., W., "Data from prostate-mri," *The Cancer Imaging Archive* (2016).

[101] Wang, X., Peng, Y., Lu, L., Lu, Z., Bagheri, M., and Summers, R. M., "Chestx-ray8: Hospital-scale chest x-ray database and benchmarks on weakly-supervised classification and localization of common thorax diseases," in [*Proceedings of the IEEE conference on computer vision and pattern recognition*], 2097–2106 (2017).

[102] Bien, N., Rajpurkar, P., Ball, R. L., Irvin, J., Park, A., Jones, E., Bereket, M., Patel, B. N., Yeom, K. W., Shpanskaya, K., et al., "Deep-learning-assisted diagnosis for knee magnetic resonance imaging: development and retrospective validation of mrnet," *PLoS medicine* **15**(11), e1002699 (2018).

[103] Consortium, N. C. I. C. P. T. A., "Radiology data from the clinical proteomic tumor analysis consortium clear cell renal cell carcinoma [cptac-ccrcc] collection [data set].," *The Cancer Imaging Archive* (2018).

[104] Heller, N., Isensee, F., Maier-Hein, K. H., Hou, X., Xie, C., Li, F., Nan, Y., Mu, G., Lin, Z., Han, M., et al., "The state of the art in kidney and kidney tumor segmentation in contrast-enhanced ct imaging: Results of the kits19 challenge," *Medical Image Analysis* **67**, 101821 (2019).

[105] Consortium, N. C. I. C. P. T. A., "Radiology data from the clinical proteomic tumor analysis consortium lung squamous cell carcinoma [cptac-lscc] collection [data set].," *The Cancer Imaging Archive* (2018).

[106] Moen, T. R., Chen, B., Holmes III, D. R., Duan, X., Yu, Z., Yu, L., Leng, S., Fletcher, J. G., and McCollough, C. H., "Low dose ct image and projection dataset," *Medical Physics* (2020).

[107] Consortium, N. C. I. C. P. T. A., "Radiology data from the clinical proteomic tumor analysis consortium lung adenocarcinoma [cptac-luad] collection [data set].," *The Cancer Imaging Archive* (2018).

[108] Consortium, N. C. I. C. P. T. A., "Radiology data from the clinical proteomic tumor analysis consortium pancreatic ductal adenocarcinoma [cptac-pda] collection [data set].," *The Cancer Imaging Archive* (2018).

[109] Yorke, A., Sala, I., Solis, D., and Guerrero, T., "A statistically characterized reference data set for image registration of pelvis using combinatorial affine registration optimization," in [*MEDICAL PHYSICS*], **46**(6), E340–E340, WILEY 111 RIVER ST, HOBOKEN 07030-5774, NJ USA (2019).

[110] Madhavi, P., Patel, S., and Tsao, A. S., "Data from anti-pd-1 immunotherapy lung [data set].," *The Cancer Imaging Archive* (2019).

[111] Hylton, N. M., Gatsonis, C. A., Rosen, M. A., Lehman, C. D., Newitt, D. C., Partridge, S. C., Bernreuter, W. K., Pisano, E. D., Morris, E. A., Weatherall, P. T., et al., "Neoadjuvant chemotherapy for breast cancer: functional tumor volume by mr imaging predicts recurrence-free survival—results from the acrin 6657/calgb 150007 i-spy 1 trial," *Radiology* **279**(1), 44–55 (2016).

[112] Fedorov, A., Clunie, D., Ulrich, E., Bauer, C., Wahle, A., Brown, B., Onken, M., Riesmeier, J., Pieper, S., Kikinis, R., et al., "Dicom for quantitative imaging biomarker development: a standards based approach to sharing clinical data and structured pet/ct analysis results in head and neck cancer research," *PeerJ* **4**, e2057 (2016).

[113] Kirk, S., Lee, Y., Sadow, C. A., and Levine, S., "Radiology data from the cancer genome atlas rectum adenocarcinoma [tcga-read] collection," *The Cancer Imaging Archive* (2016).

[114] Kurdziel, K. A., Shih, J. H., Apolo, A. B., Lindenberg, L., Mena, E., McKinney, Y. Y., Adler, S. S., Turkbey, B., Dahut, W., Gulley, J. L., et al., "The kinetics and reproducibility of 18f-sodium fluoride for oncology using current pet camera technology," *Journal of Nuclear Medicine* **53**(8), 1175–1184 (2012).

[115] Scarpace, L., Flanders, A. E., Jain, R., Mikkelsen, T., and Andrews, D. W., "Data from rembrandt," *The Cancer Imaging Archive* **10**, K9 (2015).

[116] Rajpurkar, P., Irvin, J., Bagul, A., Ding, D., Duan, T., Mehta, H., Yang, B., Zhu, K., Laird, D., Ball, R. L., et al., "Mura: Large dataset for abnormality detection in musculoskeletal radiographs," *arXiv preprint arXiv:1712.06957* (2017).